Journal of Materials Science & Technology 34 (2018) 1730–1738

Contents lists available at ScienceDirect

Journal of Materials Science & Technology

journal homepage: www.jmst.org

Constitutive equation and model validation for a 31 vol.% B_4Cp/6061Al composite during hot compression

L. Zhou [a,b], C. Cui [c], Q.Z. Wang [a,*], C. Li [d], B.L. Xiao [a,*], Z.Y. Ma [a]

[a] Institute of Metal Research, Chinese Academy of Sciences, Shenyang 110016, China
[b] School of Electromechanical and Vehicle Engineering, Yantai University, Yantai 264005, China
[c] School of Mechanical Engineering, Shenyang Ligong University, Shenyang 110159, China
[d] Nuclear and Radiation Safety Center, Ministry of Environmental Protection, Beijing 100082, China

ARTICLE INFO

Article history:
Received 23 August 2017
Received in revised form 6 December 2017
Accepted 26 December 2017
Available online 14 February 2018

Keywords:
Composites
B_4C/Al
Constitutive equation
Hot compression
Finite element simulation

ABSTRACT

An accurate constitutive equation is essential to understanding the flow behavior of B_4C/Al composites during the hot deformation. However, the constitutive equations developed previously in literature are generally for low strain rate deformation. In the present work, we modified the general constitutive equation and take the high strain rate correction into account. The constitutive equation for a 31 vol.% B_4Cp/6061Al composite was constructed based on the flow stresses measured during isothermal hot compression at temperatures ranging from 375 to 525 °C and strain rates from 0.01 to 10 s^{-1}. The experimental flow stresses were corrected by considering temperature-dependent Arrhenius factor. The modified equation was then verified by using DEFORM-3D finite element analysis to simulate the experimental hot compression process. The results show that the modified equation successfully predicts flow stress, load–displacement, and the temperature rise. This helps to optimize the hot deformation process, and to obtain desirable properties, such as reduced porosity and homogenous particle distribution in B_4C/Al composites.

© 2018 Published by Elsevier Ltd on behalf of The editorial office of Journal of Materials Science & Technology.

1. Introduction

B_4C/Al composites possess excellent physical and mechanical properties; they are light weight, have high wear resistance and thermal stability, and have an excellent capacity for neutron absorption. Therefore, they are increasingly used in the automotive, military, and especially nuclear industries, for the storage and transportation of spent fuels [1–3]. In recent years, extensive work has been carried out to investigate B_4C/Al composite fabrication methods [4–6], microstructures [3,5], and how the microstructure influences the mechanical properties [7].

In order to reduce porosity and to obtain a more homogenous particle distribution, thermo-mechanical treatments, such as forging, extrusion and hot rolling are essential. However, because the mechanical properties of the B_4C particles (B_4Cp) are completely different from those of the Al alloy matrix, the hot deformation behavior of B_4C/Al composites is very different from that of traditional metals. Both experimental and numerical methods have been used to investigate the effect of the microstructure on the macroscopic deformation and fracture properties of particle reinforced metal matrix composites. These studies show that the particles play an important role in load bearing, and that deformation of the composite is much harder than of the matrix Al alloy [8–10]. Therefore, it is necessary to understand the flow behavior of B_4C/Al composites under the typical temperatures and strain rates encountered during the hot deformation process.

Constitutive equations can effectively predict a material's flow behavior based on a limited amount of experimental data, which can then be used in finite element code to simulate deformation of the material under specified loading conditions [11]. Experimental tests have been carried out to develop constitutive equations for particle reinforced metal matrix composites. For example, Wang et al. [12] developed a modified viscoplastic constitutive equation to describe the hot deformation behavior of short carbon fiber (Csf) reinforced magnesium matrix composites (Csf/AZ91D) by means of compression tests. This model successfully predicted the strain softening of composites undergoing severe plastic deformation. Spigarelli et al. [13] and Luan et al. [14] established constitutive relations for Al_2O_3/Al composites, utilizing torsion and hot compression tests. The obtained phenomenological constitutive

* Corresponding authors.
E-mail addresses: qzhwang@imr.ac.cn (Q.Z. Wang), blxiao@imr.ac.cn (B.L. Xiao).

https://doi.org/10.1016/j.jmst.2018.02.001
1005-0302/© 2018 Published by Elsevier Ltd on behalf of The editorial office of Journal of Materials Science & Technology.

equation [13] can be used to simulate hot deformation as well as creep behavior of the composite. SiCp/Al composites have drawn much attention in recent years, and constitutive equations for their deformation behavior have been developed [15–18]. It was found that a processing map could be used to determine the optimum strain rate and temperature for the hot deformation of SiCp/Al [15–17]. In our previous study [18], an Arrhenius-type constitutive equation for a 17 vol.% SiCp/2009Al composite was presented by using hot compression tests, and then implemented into finite element software, which successfully predicted the hot rolling process of the composite.

Most studies regarding the hot deformation behavior of metal matrix composites have investigated only deformation at low strain rates ($\leq 1\ s^{-1}$) [19,20], whereas during the hot rolling process, the material actually undergoes large plastic deformation, and the strain rate is often larger than $1\ s^{-1}$ [21,22]. With a high enough strain rate, the actual temperature of a specimen may be inhomogeneous, deviating from the preset temperature due to the heat generated by the large plastic deformation. Therefore, measured stresses are inappropriate for constitutive analysis of the material without correction [23]. However, few studies have dealt with this flow stress correction at high strain rates for composites, which leads to poor accuracy of the constitutive equation.

Compared to other composites, investigations on the hot workability of B_4C/Al composites are very limited. Gangolu et al. [24] studied the hot deformation of an as-cast 5 wt% B_4C/A356 composite by compression tests, and the constitutive relationship and processing map were established. Li et al. [25] reported that the processing map based on Gegel's criterion could effectively predict the material behavior of a 20 vol.% B_4C/6061Al composite, allowing the optimum parameters for hot working to be obtained. Similar to the cases mentioned above, the strain rate in question in these studies was quite low.

In the present work, in order to accurately describe the hot deformation of B_4C/Al composites under high strain rates, we modified the general constitutive relationship by including the flow stress correction at higher strain rates. Hot compression tests of B_4Cp/6061Al composites were carried out at a wide range of temperatures and strain rates. The flow stresses under relatively high strain rates, measured experimentally, were corrected. Then, the constitutive constants of the Arrhenius-type equations, based on both the experimental and the corrected data, were determined. In order to validate the proposed constitutive equation, it was implemented into the finite element software DEFORM-3D to simulate the hot compression process.

This paper is arranged as follows. In Section 2, we carried out uniaxial hot compression tests to obtain stress–strain curves. In Section 3, the measured stresses were checked and corrected, and the constitutive constants of the Arrhenius-type equations were determined using the corrected stresses. In Section 4, the established constitutive relationship was validated by comparison of flow stress, load–displacement, and temperature rise with their measured values in compression tests. Finally in Section 5, we summarize the main results of this work.

2. Experimental

Generally, the stress–strain data used to determine constitutive models are obtained by employing uniaxial tension or compression tests. Since larger strains can be achieved with compression tests, this is currently the more widely used method [26]. Therefore, in the present work, we utilized compression tests to get the stress–strain data.

A 31 vol.% B_4Cp/6061Al composite was fabricated by the powder metallurgy technique, which involves the mixing of 6061Al and B_4C powders, cold compaction and hot-pressing of the mixture powders, and hot-rolling [27]. 6061Al powders (Al–1.0Mg–0.65Si–0.25Cu, wt.%) and B_4C particles with an average diameter of 7 μm were selected as the raw materials. The initial microstructure of the rolled 31 vol.% B_4Cp/6061Al composite is shown in Fig. 1.

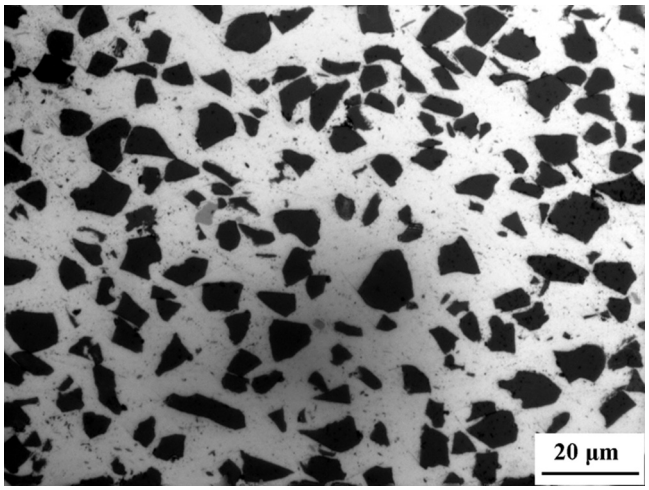

Fig. 1. Optical micrograph of the 31 vol.% B_4Cp/6061Al composite.

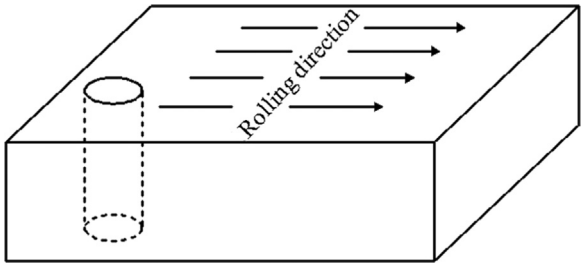

Fig. 2. Schematic of the position of a hot compression specimen in the hot-rolled plate.

A series of cylindrical specimens, 8 mm in diameter and 12 mm in height, were machined from a hot-rolled plate, as shown in Fig. 2. Isothermal hot compression tests were performed with a Gleeble-3800 thermal simulator in the temperature range of 375–525 °C at 25 °C intervals, and strain rates of 0.01, 0.1, 1 and $10\ s^{-1}$. In order to reduce the influence of friction on deformation, graphite lubricant was applied to the top and bottom surfaces of the specimens. Thermocouples were welded at the mid-height of the specimen's surface to measure the temperature.

The detail of the experimental procedure of the hot compression test is shown in Fig. 3. Before compression, the specimen was heated to a preset temperature at a heating rate of 5 °C/s, and held for 10 min to obtain a uniform temperature field. All specimens were compressed to a true strain of 0.69, and then water quenched immediately.

3. Results and discussion

3.1. Flow stress analysis

Fig. 4 shows true stress–true strain curves of the 31 vol.% B_4Cp/6061Al composite. The flow stress increased with decreasing temperature or with increasing strain rate, and work hardening and flow softening occurred simultaneously during the hot deformation process. In the initial stage of the deformation, the flow stress rapidly increased due to work hardening. After reaching a

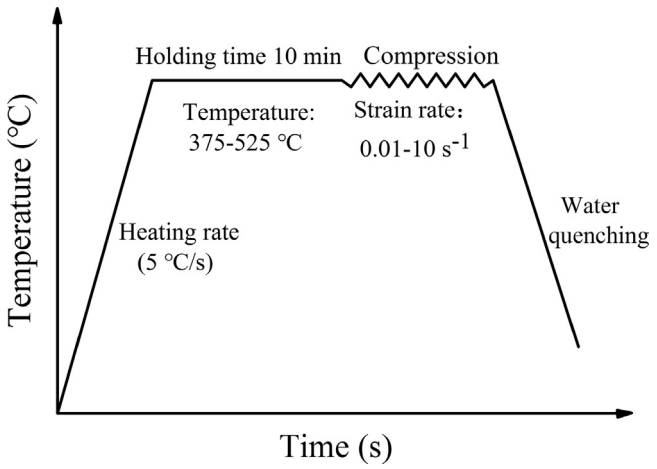

Fig. 3. Experimental procedure of hot compression.

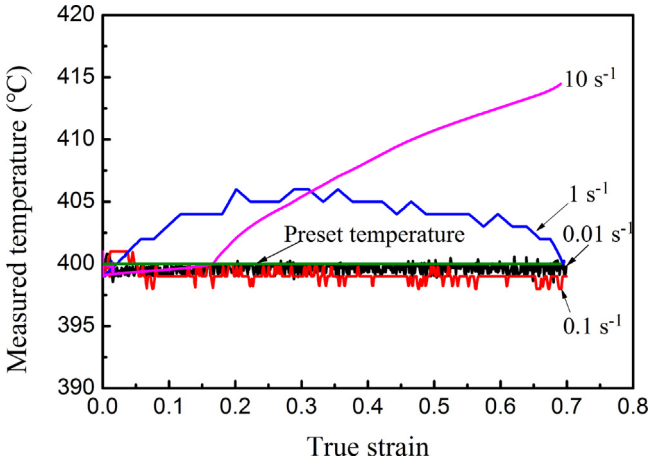

Fig. 5. Measured temperature changes of hot compressed specimens with true strain at 400 °C for different strain rates.

peak value, the flow stress gradually decreased to a relatively steady state and was no longer dependent on the strain, especially at high temperatures and low strain rates.

Fig. 4 illustrates that when the temperature was higher than or equal to 475 °C, or when the strain rate was lower than or equal to 0.1 s^{-1}, flow softening was not obvious. Furthermore, it is interesting to note that there was significant oscillation of the flow stress curve at a higher strain rate (10 s^{-1}), which might be associated with inhomogeneous deformation or micro-cracking. Similar behavior has been reported in other metal materials [28].

3.2. Correction of flow stress

Ideally, a dynamic equilibrium between the heating supply and energy dissipation would be maintained by closed-loop control of the thermal simulator, thus keeping the temperature of the specimen constant during the compression process. However, under high-speed deformation conditions, the temperature rise for plastic deformation cannot be ignored. Unfortunately, this rise in temperature cannot be measured in real time owing to the hysteresis effect of thermocouple and, and therefore, the equilibrium state is broken.

Fig. 5 shows how the measured temperature of the hot compressed specimens changes with true strain, at a preset temperature of 400 °C for different strain rates. It should be noted that at strain rates of 0.01 and 0.1 s^{-1}, the measured temperatures were identical to the preset temperatures. In these cases, the flow stresses can be used directly for calculating the constitutive constants.

When the strain rate increased to 1 s^{-1}, the temperature of specimen increased in the initial stage and then gradually decreased to the preset temperature. This is because the response time of thermocouple is 0.1 s, and the deformation duration is long enough that the heat generated from plastic deformation is able to dissipate at strain rates of less than or equal to 1 s^{-1} [23]. Therefore, flow stresses at the strain rate of 1 s^{-1} need to be corrected due to the slight deviation of the actual temperature from the preset value.

Compared to the lower strain rates, at the strain rate of 10 s^{-1} the deformation speed was so rapid that the thermocouples could not measure the actual temperature of the specimen because their response time is longer than the deformation duration. The heating system cannot react synchronously to the changing temperatures, which leads to inhomogeneous deformation and a remarkable temperature increase in the specimens. Therefore, flow stresses at higher strain rates should be corrected.

The Arrhenius equation is widely used to describe the dependence of flow stress on temperature and strain rate in the hot deformation process [29,30]. The equation can be written as

$$\dot{\varepsilon} = Af(\sigma)\exp\left(-\frac{Q}{RT}\right) \tag{1}$$

and

$$f(\sigma) = \begin{cases} \sigma^{n_1} & \alpha\sigma < 0.8 \\ \exp(\beta\sigma) & \alpha\sigma > 1.2 \\ [\sinh(\alpha\sigma)]^n & \text{for all } \sigma \end{cases} \tag{2}$$

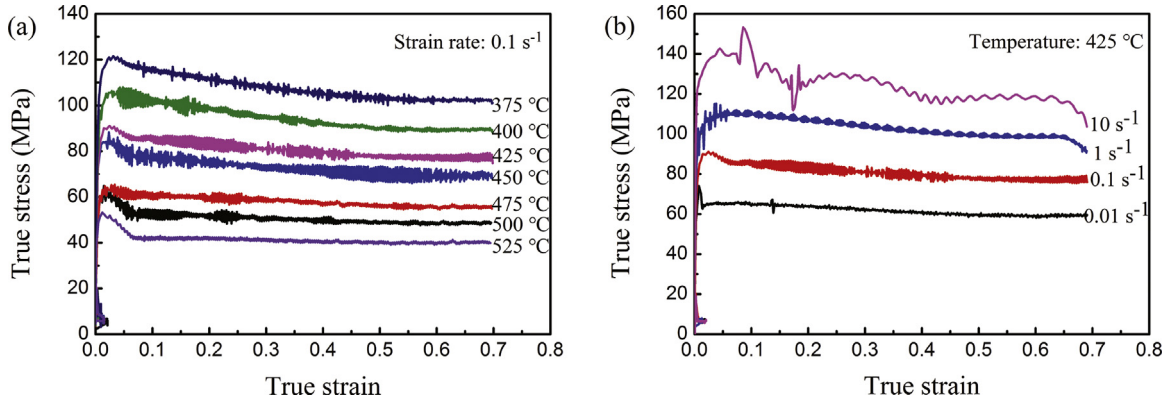

Fig. 4. True stress–true strain curves of the 31 vol.% B_4C_p/6061Al composite at (a) 0.1 s^{-1} for different temperatures and (b) 425 °C for different strain rates.

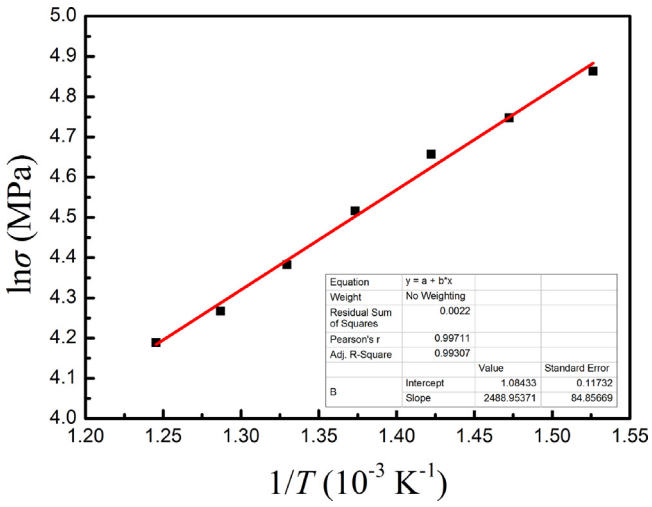

Fig. 6. Relationship between ln σ and 1/T at strain rate of 1 s^{-1}.

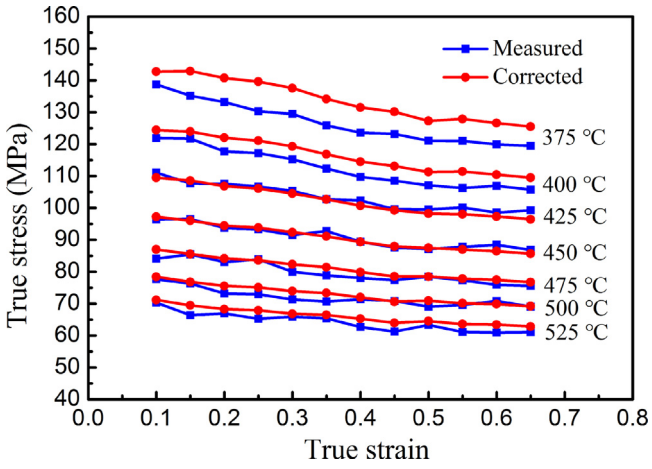

Fig. 7. Experimental flow stresses and corrected stresses of 12 strain points at a strain rate of 1 s^{-1}.

where σ is the flow stress (MPa), $\dot{\varepsilon}$ is the strain rate (s^{-1}), A, β, n_1, α and n are material constants, with $\alpha = \beta/n_1$, R is the universal gas constant (8.314 J/mol K^{-1}), T is the absolute temperature (K), and Q is the activation energy (J/mol).

At a strain rate of 1 s^{-1}, when substituting the first expression in Eq. (2) into Eq. (1), the following constitutive equation is obtained:

$$\dot{\varepsilon} = A\sigma^{n_1} \exp\left(-\frac{Q}{RT}\right) \tag{3}$$

Taking logarithms of both sides of Eq. (3) gives:

$$\ln\sigma = \frac{Q}{nR}\cdot\frac{1}{T} + \frac{\ln\dot{\varepsilon} - \ln A}{n_1} \tag{4}$$

For the strain rate of 1 s^{-1}, the linear fitting of experimental flow stress (lnσ) and temperature (1/T) is plotted in Fig. 6. The relationship can be expressed as:

$$\ln\sigma = 2488.95/T + 1.084 \tag{5}$$

By substituting the preset temperature into Eq. (5) for true strains from 0.1 to 0.69 at intervals of 0.05, the flow stresses were corrected. The experimental flow stresses and temperature corrected stresses of the 12 strain points at different temperatures are shown in Fig. 7. It can be seen that the corrected flow stresses are slightly higher than the experimental ones, especially at lower temperatures.

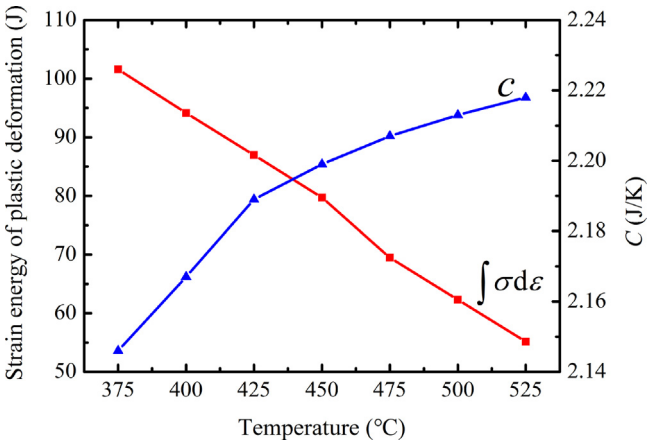

Fig. 8. $\int \sigma d\varepsilon$ and C at different temperatures.

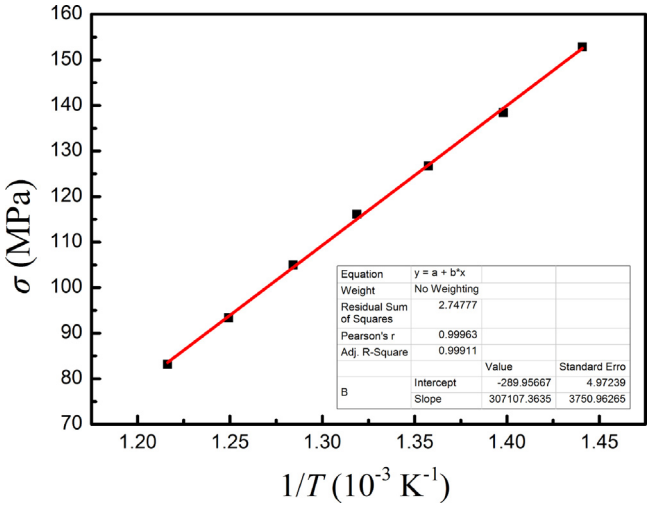

Fig. 9. Relationship between σ and 1/T at strain rate of 10 s^{-1}.

At a strain rate of 10 s^{-1}, when substituting the second expression in Eq. (2) into Eq. (1), the constitutive equation is expressed as:

$$\dot{\varepsilon} = A\exp(\beta\sigma)\exp\left(-\frac{Q}{RT}\right) \tag{6}$$

Taking logarithms of both sides of Eq. (6) gives:

$$\sigma = \frac{Q}{\beta R}\cdot\frac{1}{T} + \frac{\ln\dot{\varepsilon} - \ln A}{\beta} \tag{7}$$

where T is the true temperature, and can be calculated by the following equation:

$$T = T_{pre} + \Delta T \tag{8}$$

where T_{pre} is the preset temperature, and ΔT is the temperature rise during deformation. The temperature rise ΔT in the deformed region of the specimen can be calculated according to the law of energy conservation [28]:

$$\Delta T = \frac{\eta\int\sigma d\varepsilon}{C} \tag{9}$$

where η is the efficiency of heat transformation (in this study η = 0.97) [31], $\int\sigma d\varepsilon$ is the strain energy of plastic deformation (J), and C is the heat capacity (J K^{-1}). $\int\sigma d\varepsilon$ and C vary greatly with temperature, as shown in Fig. 8.

From Eq. (7), for a fixed strain rate, the experimental flow stress σ is proportional to 1/T; the linear relationship can be fitted from

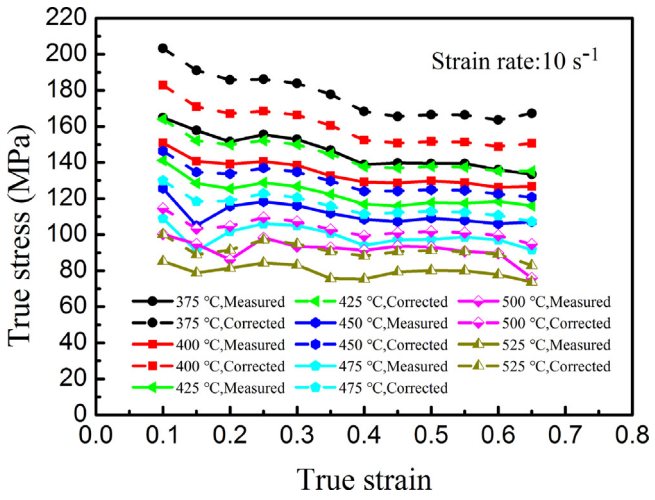

Fig. 10. Experimental flow stresses and corrected stresses of 12 strain points at a strain rate of 10 s^{-1}.

the experimental stresses σ and calculated true temperatures T at different strains. Fig. 9 shows the linear line fitting for σ against $1/T$ at a strain of 0.3, with the relationship between σ and $1/T$ written as

$$\sigma = 307107.363/T - 289.956 \quad (10)$$

By substituting the true temperature into Eq. (10) for true strains from 0.1 to 0.69 at intervals of 0.05, the flow stresses were corrected. Fig. 10 shows the comparison between experimental flow stresses and the temperature corrected stresses at the strain rate of 10 s^{-1} for different temperatures. It can be seen that the corrected flow stresses are much higher than the measured ones, especially at lower temperatures. Compared to at a strain rate of 1 s^{-1} (see Fig. 7), it can be found that the temperature rise has a more significant effect on experimental flow stress at higher strain rates. Similar results were found for other materials by Xiao et al. [32].

3.3. Determination of material constants of the constitutive equations

Most of the experimental true stress–true strain curves of the 31 vol.% B_4Cp/6061Al composite reach a steady state by a true strain of around 0.3. In order to obtain accurate material constants for the constitutive equations, the effect of strain on the constitutive constants is considered. A total of 12 strains were investigated, from 0.1 to 0.69 at intervals of 0.05. The strain of 0.3 was selected as an example to describe the calculation procedure. The flow stresses at a strain of 0.3 are listed in Table 1.

When the effect of temperature on flow stress is neglected, for low and high stress levels, substituting the power law and the exponential law of $f(\sigma)$ in Eq. (2) into Eq. (1), gives the following relationships, respectively:

$$\dot{\varepsilon} = B\sigma^{n_1} \quad (11)$$

$$\dot{\varepsilon} = C\exp(\beta\sigma) \quad (12)$$

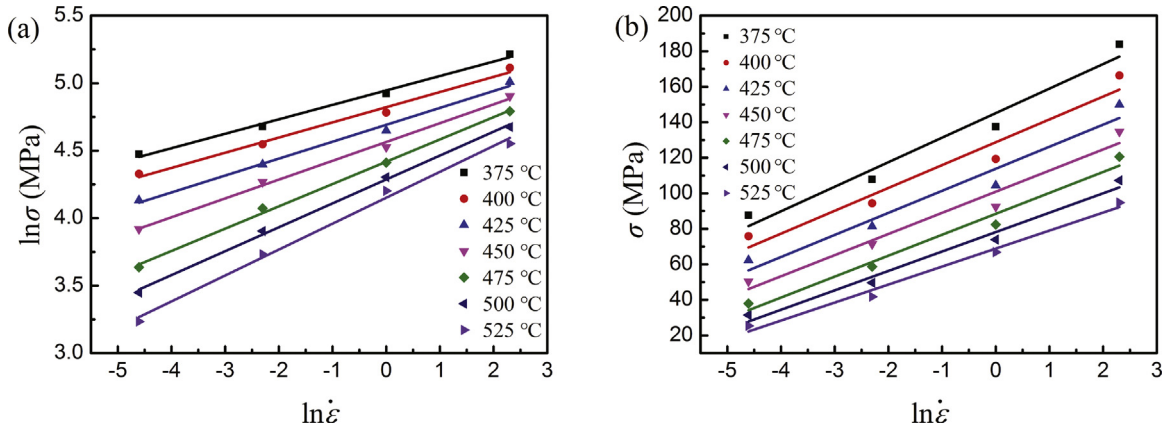

Fig. 11. Evaluation of (a) n_1 by fitting ln σ vs ln $\dot{\varepsilon}$, and (b) β by fitting σ vs ln $\dot{\varepsilon}$.

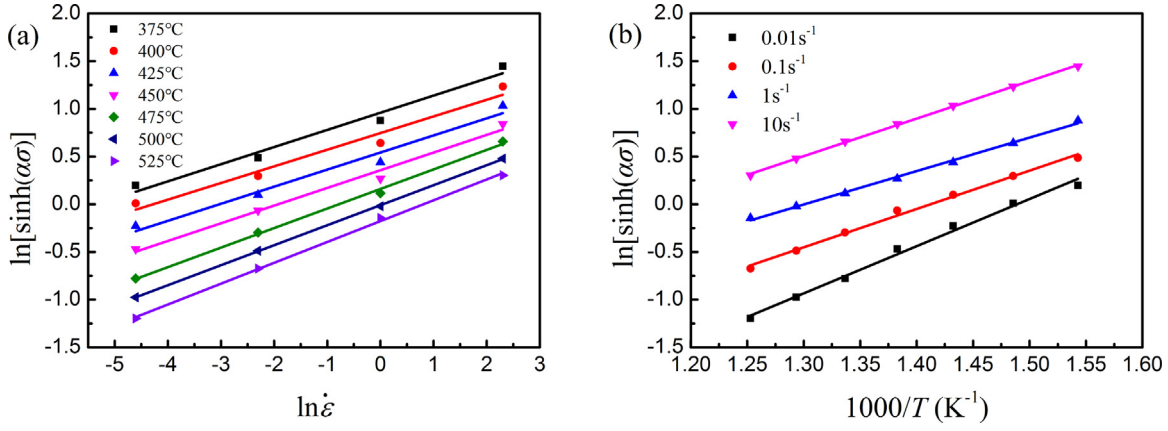

Fig. 12. Evaluation of (a) n by fitting ln[sinh($\alpha\sigma$)] vs ln $\dot{\varepsilon}$, and (b) Q by fitting ln[sinh($\alpha\sigma$)] vs 1000/T.

Table 1
Flow stresses at a strain of 0.3 under different deformation conditions (MPa).

Strain rate (s^{-1})	Temperature (°C)						
	375	400	425	450	475	500	525
0.01	87.73	75.84	62.31	50.38	37.94	31.46	25.39
0.1	107.83	94.38	81.36	71.30	58.72	49.60	41.79
1	129.50	115.31	105.33	91.50	80.01	71.34	65.95
10	152.83	138.42	126.74	116.09	104.97	93.37	83.13

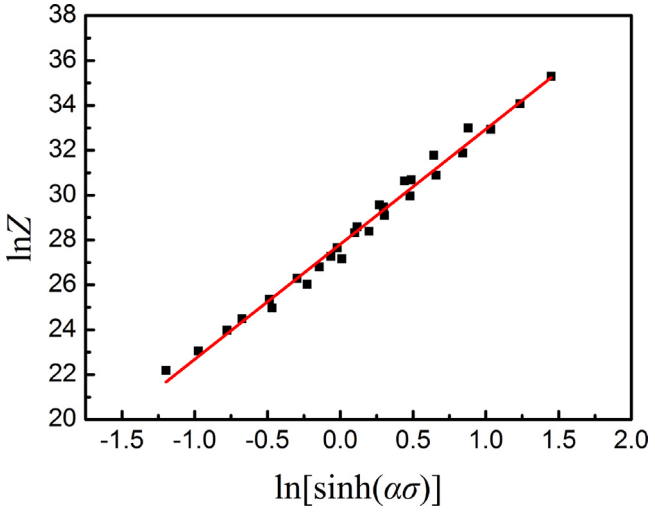

Fig. 13. Fitting of ln Z vs ln[sinh($\alpha\sigma$)] for calculating ln A.

where B and C are material constants. Taking logarithms of Eqs. (11) and (12), they can be written as:

$$\ln\dot{\varepsilon} = n_1 \ln\sigma + \ln B \tag{13}$$

$$\ln\dot{\varepsilon} = \beta\sigma + \ln C \tag{14}$$

The values of $1/n_1$ and $1/\beta$ are the average slopes of the lnσ vs ln $\dot{\varepsilon}$ curves in Fig. 11(a) and the σ vs ln $\dot{\varepsilon}$ curves in Fig. 11(b), respectively. The constants n_1 and β are fitted as 7.185 and 0.084, respectively; this gives the value of $\alpha = \beta/n_1 = 0.0117$.

For all stress levels, Eq. (1) is rewritten as

$$\dot{\varepsilon} = A[sinh(\alpha\sigma)]^n \exp(-\frac{Q}{RT}) \tag{15}$$

Table 2
Calculated material constants of the Arrhenius constitutive equation for the 31 vol.% B4Cp/6061Al composite.

Constant	Q (kJ/mol)	ln$A$	n	α (MPa^{-1})
Value	177.79	27.8	5.21	0.0117

By taking logarithms and rearranging Eq. (15), the following equation is obtained:

$$\ln[sinh(\alpha\sigma)] = \frac{\ln\dot{\varepsilon}}{n} + \frac{Q}{nRT} - \frac{\ln A}{n} \tag{16}$$

In the same way, the values of n and activation energy Q can be obtained from the slope of the linear fitting lines of ln[$sinh(\alpha\sigma)$] vs ln $\dot{\varepsilon}$ and ln[$sinh(\alpha\sigma)$] vs 1000/T, respectively. Form Fig. 12, the average values of n and Q were calculated to be 5.21 and 177.79 kJ/mol respectively. The value for Q is close to that reported by Li et al. for the same composite (185.62 kJ/mol) [33].

Furthermore, the effects of temperature and strain rate on the material's deformation behavior can be represented by the Zener–Holloman (Z) parameter, and expressed either by exponential law or the hyperbolic sine law as follows [34,35]:

$$Z = \dot{\varepsilon}\exp(\frac{Q}{RT}) \tag{17}$$

$$Z = A\sinh(\alpha\sigma)^n \tag{18}$$

Taking logarithms of both sides of Eq. (18) gives:

$$\ln Z = n\ln[\sinh(\alpha\sigma)] + \ln A \tag{19}$$

Then, by substituting values of Q at different temperatures and strain rates into Eq. (17), the parameters Z and ln$Z$ can be obtained. The relationship between ln[sinh($\alpha\sigma$)] and ln$Z$ is shown in Fig. 13, and the intercept of the fitting line is ln$A$ = 27.8.

Based on experimental data and the results obtained above, all material constants of the Arrhenius constitutive equation were calculated at a true strain of 0.3 and are listed in Table 2. From Eq. (18), the flow stress (σ) can be written as a function of the Zener–Holloman parameter. Therefore, at a particular strain, the established constitutive relationship can be summarized as follows:

$$\sigma = \frac{1}{\alpha}\ln\left\{\left(\frac{Z}{A}\right)^{1/n} + \left[\left(\frac{Z}{A}\right)^{2/n} + 1\right]^{1/2}\right\} \tag{20}$$

Using Eq. (20), the flow stress of the 31 vol.% B_4Cp/6061Al composite was calculated at different temperatures and strain rates. Fig. 14 compares the experimental flow curves with those calculated by using the Arrhenius constitutive equation under different

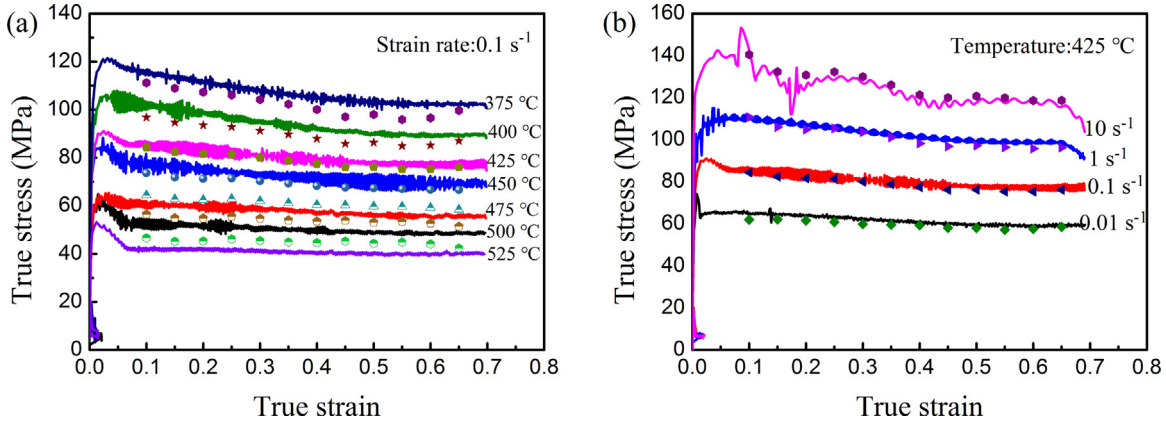

Fig. 14. Comparison between the calculated and experimental flow stress curves at (a) a strain rate of 0.1 s^{-1} for different temperatures and (b) 425 °C for different strain rates.

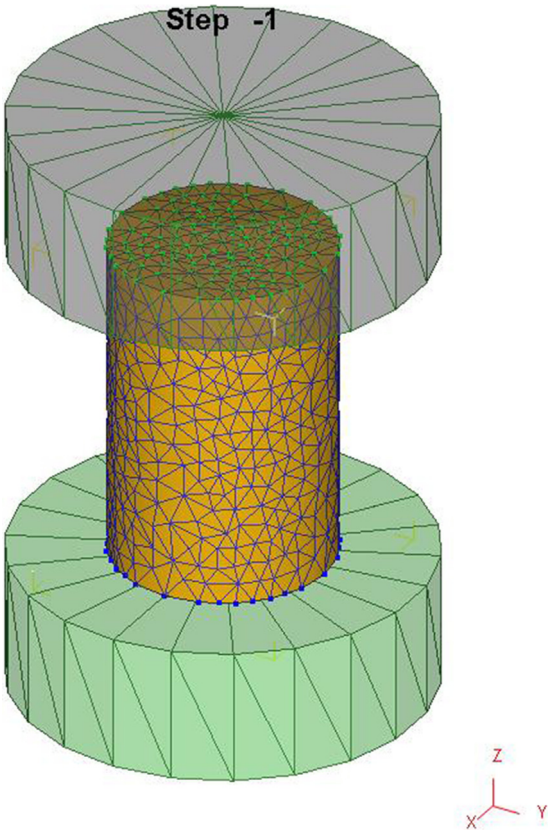

Fig. 15. Three-dimensional finite element model.

strain rates for seven testing temperatures. It can be seen that the predicted data are in good agreement with the experimental ones.

4. Finite element verification

Although the established constitutive equation can give an accurate prediction of the flow stress for the 31 vol.% B_4Cp/Al composite during hot compression, the rationality of the constitutive equation depends not only on the accuracy of the description of flow stress but also on the reliability of the numerical simulation. To verify the reliability of the presented constitutive equation, a finite element model of the same size as in the experiment was developed using DEFORM-3D finite element software; the Arrhenius constitutive

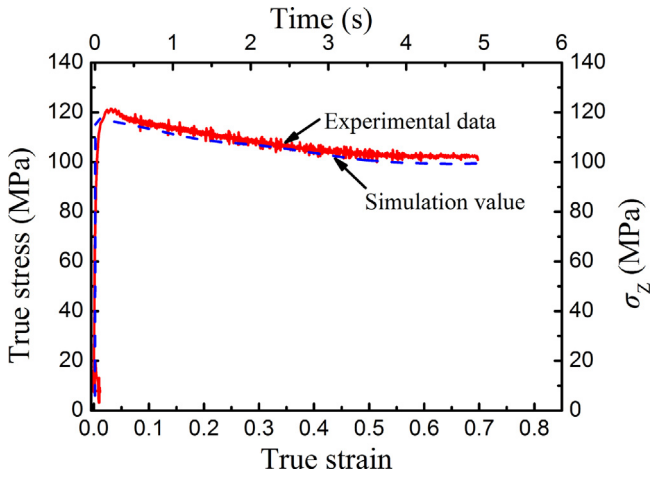

Fig. 17. Comparison between experimental flow stress and stress (σ_z) calculated by FEM.

equations with the determined material parameters were embedded into a rate-dependent plasticity material model. As shown in Fig. 15, the cylindrical workpiece was defined as a plastic body and the two dies were defined as isothermal rigid bodies.

Hot compression tests were numerically simulated by using a nonlinear thermo-mechanical coupled finite element method (FEM); the true stress–true strain property, force–displacement curve and the temperature rise under different experimental conditions were calculated.

In this model, both the thermal and displacement boundary conditions were defined. The initial temperatures of the workpiece and dies were set to a preset temperature, and the heat transfer coefficient between the workpiece and dies, and the workpiece and air were set to 25 and 0.02 kW/(m^2 K), respectively. A constant shear friction model with a friction factor of 0.3 was used for the friction modeling [27]. The lower die was constrained against movement in any direction at the bottom, and the speed of the upper die was calculated as follows:

$$v = \frac{S}{t} = \frac{S}{\varepsilon/\dot{\varepsilon}} \tag{21}$$

where S is the total displacement of the workpiece (mm), t is the compression time, and ε and $\dot{\varepsilon}$ are strain and strain rate, respectively.

Fig. 16 shows the distribution of stress in the compression direction at a temperature of 375 °C and a strain rate of 0.1 s^{-1}. Fig. 16(a)

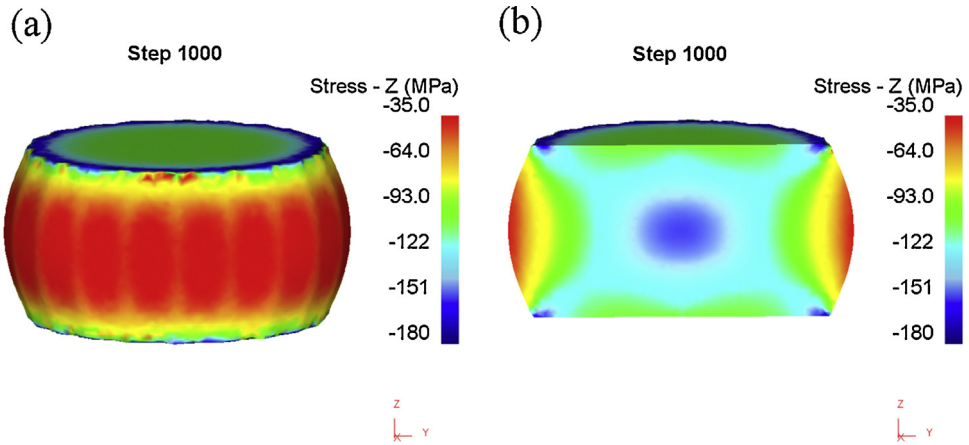

Fig. 16. Stress (σ_z) distribution by FEM, calculated at a temperature of 375 °C and a strain rate of 0.1 s^{-1}, of (a) the whole model and (b) the vertical section along the compression direction.

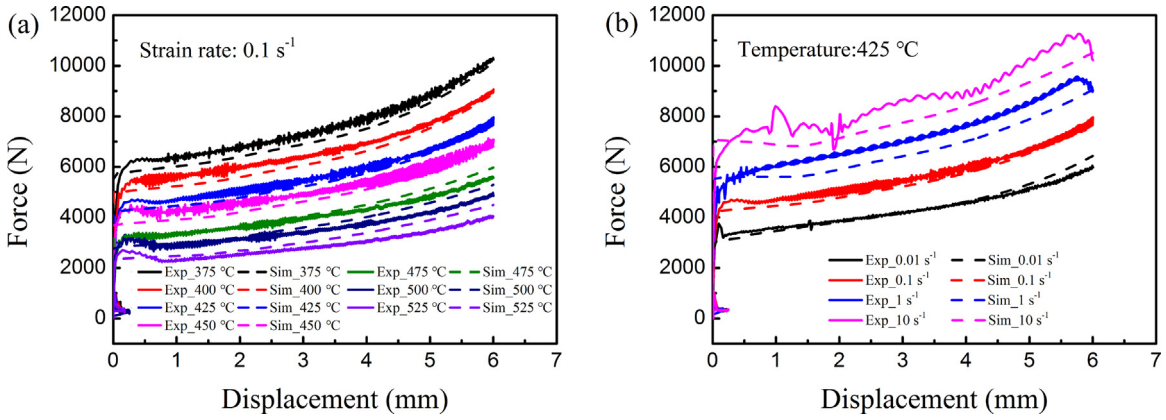

Fig. 18. Comparison between experimental and simulated force–displacement curves during hot compression, at (a) a strain rate of 0.1 s^{-1}, and (b) a temperature of 425 °C.

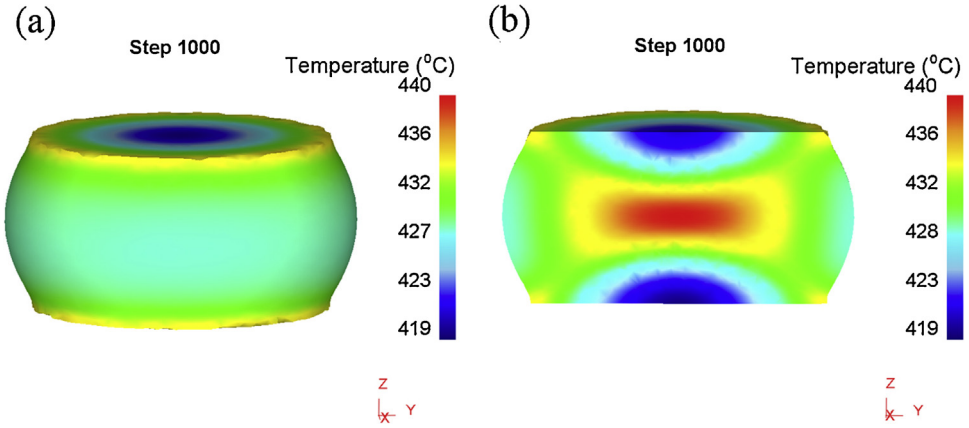

Fig. 19. Distribution of temperature at a strain rate of 10 s^{-1} and a temperature of 375 °C, of (a) the whole model and (b) the vertical section along the compression direction.

and (b) shows the whole model and the vertical section along the compression direction, respectively. It can be seen that the distribution of stress is very uniform, with two high compressive stress regions, in the center and edge of the specimen. The true stress outputted in the hot compression experiment is the average stress; the average stress in the compression direction (σ_Z), and the strain (ε_Z) of the model, can be obtained from the following equations [8]:

$$\sigma_Z = \frac{\sum_1^m V_i \sigma_i}{\sum_1^m V_i} \tag{22}$$

$$\varepsilon_Z = \ln \frac{l+U}{l} \tag{23}$$

where m is the number of elements in the workpiece, σ_i and V_i are the stress in the compression direction and volume of each element, respectively. l is the original length of the workpiece, and U is the displacement of the loading surface.

By these calculations, the absolute value of stress can be obtained. Fig. 17 compares the experimental and simulated true stress–true strain curves during hot compression; it can be seen that the computational strain–stress curve agreed well with the experimental one.

Fig. 18 compares the predicted force–displacement curves with the experimental curves. It can be seen that most of the predicted force–displacement curves match the measured ones well for the whole hot compression process, except for deformation at the higher strain rates, i.e. at 1 s^{-1} and 10 s^{-1} (see Fig. 18(b)). Fig. 18(a) shows that when the temperature is higher than or equal to 475 °C, the simulated values are larger than the experimental values, while at temperatures lower than 475 °C, the simulated values are smaller

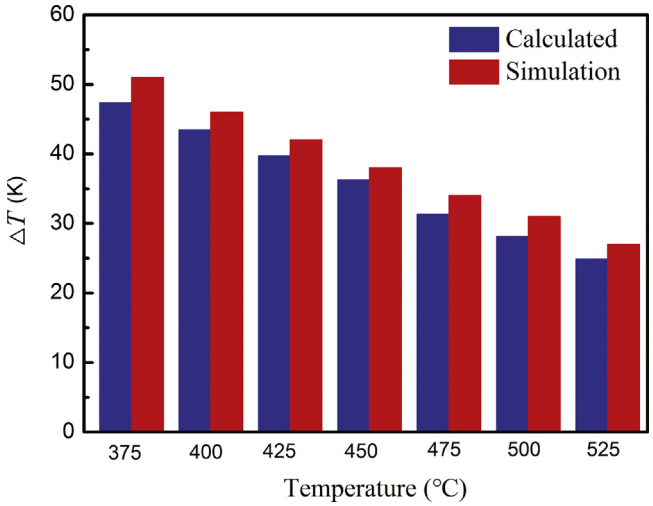

Fig 20. Comparison of the temperature rise ΔT at a strain rate of 10 s^{-1}, between the theoretical calculation and FEM simulation.

than the experimental values. This is consistent with the trend in Fig. 14, and the reason is that the variation of flow stress is different for high or low temperatures, or high or low strain rates (see Fig. 4).

Fig. 19 shows the temperature field at a preset temperature of 375 °C and a strain rate of 10 s^{-1}. Fig. 19(a) and (b) shows the whole model and the vertical section along the compression direction, respectively. It is clear that the true temperature field of the specimen is very inhomogeneous; the internal temperature of the

specimen is higher than the surface temperature due to the heat generated by plastic deformation.

Fig. 20 compares the temperature rise at a strain rate of 10 s^{-1}, between the theoretical calculation (from Eq. (9)) and the FEM simulation, at different preset temperatures. It is clear that with decreasing preset temperature, the strain energy of plastic deformation increases, and thus the temperature rise increases. At the same time, it is obvious that all of the simulation values are higher than those of the theoretical calculation; the heat generated by friction between the specimen and the anvils was neglected in the theoretical calculation. The error between the theoretical calculation and the FEM simulation is largest (9.6%) at 375 °C, which further demonstrates the higher prediction accuracy of the constitutive equation under various forming conditions.

5. Conclusions

(1) For the hot deformation of 31 vol.% B_4Cp/6061Al composites at a wide range of temperatures and strain rates, the flow stress increased with decreasing temperature or increasing strain rate, and can be expressed by Arrhenius constitutive equations.
(2) When the strain rate is equal to or less than 0.1 s^{-1}, the measured temperatures and the corresponding stresses are relatively accurate. When the strain rate is equal to or larger than 1 s^{-1}, the influence of temperature rise on the flow stress should be corrected from the experimental results. The Arrhenius constitutive constants for 31 vol.% B_4Cp/6061Al composite were obtained on the basis of the experimental and corrected data.
(3) By applying the developed constitutive equation in DEFORM-3D finite element software, the stress–strain, force–displacement and temperature responses during hot compression were simulated. There is a good consistency between the simulated and experimental results, which confirms that the current constitutive equation is reliable and feasible for numerical simulation of the deformation behavior of 31 vol.% B_4Cp/6061Al composites.

Acknowledgment

This work was financially supported by the National Natural Science Foundation of China (Grant No. U1508216).

References

[1] E. Trujillo-Vázquez, M.I. Pech-Canul, J.C. Guía-Tello, M.A. Pech-Canul, Mater. Des. 89 (2016) 94–101.
[2] K. Kalaiselvan, N. Murugan, Trans. Nonferrous Met. Soc. China 23 (2013) 616–624.
[3] S. Karabulut, H. Karakoc, R. Citak, Comp. Part B-Eng. 101 (2016) 87–98.
[4] T. Thirumalai, R. Subramanian, S. Kumaran, S. Dharmalingam, S.S. Ramakrishnan, J. Sci. Ind. Res. 73 (2014) 667–670.
[5] H.S. Chen, W.X. Wang, Y.L. Li, J. Zhou, H.H. Nie, Q.C. Wu, Mater. Des. 94 (2016) 360–367.
[6] A.G. Rao, M. Mohape, V.A. Katkar, D.S. Gowtam, V.P. Deshmukh, A.K. Shah, Mater. Manuf. Proc. 25 (2010) 572–576.
[7] C.D. Wu, K.K. Ma, J.L. Wu, P. Fang, G.Q. Luo, F. Chen, Q. Shen, L.M. Zhang, J.M. Schoenung, E.J. Lavernia, Mater. Sci. Eng. A 675 (2016) 421–430.
[8] J.F. Zhang, X.X. Zhang, Q.Z. Wang, B.L. Xiao, Z.Y. Ma, J. Mater. Sci. Technol. 34 (2018) 627–634.
[9] A. Alizadeh, E. Taheri-Nassaj, M. Hajizamani, J. Mater. Sci. Technol. 27 (2011) 1113–1119.
[10] D.S. Zhou, H.W. Geng, W. Zeng, D.L. Zhang, C. Kong, P. Munroe, J. Mater. Sci. Technol. 33 (2017) 1323–1328.
[11] X.J. Gao, Z.Y. Jiang, D.B. Wei, H.J. Li, S.H. Jiao, J. Xu, X.M. Zhang, J.T. Han, D.F. Chen, Mater. Sci. Eng. A 595 (2014) 1–9.
[12] Z.J. Wang, L.H. Qi, G. Wang, H.J. Li, M.S. Dargusch, Mech. Mater. 102 (2016) 90–96.
[13] S. Spigarelli, E. Evangelista, E. Cerri, T.G. Langdon, Mater. Sci. Eng. A 319-321 (2001) 721–725.
[14] B.F. Luan, R.S. Qiu, C.D. Li, X.F. Yang, Z.Q. Li, D. Zhang, Q. Liu, Trans. Nonferrous Met. Soc. China 25 (2015) 1056–1063.
[15] Y.L. Sun, J.P. Xie, S.M. Hao, A.Q. Wang, P. Liu, M. Li, J. Alloys Compd. 649 (2015) 865–871.
[16] S. Ramanathan, R. Karthikeyan, M. Gupta, J. Mater. Process. Technol. 183 (2007) 104–110.
[17] J.C. Shao, B.L. Xiao, Q.Z. Wang, Z.Y. Ma, Y. Liu, K. Yang, Mater. Sci. Eng. A 527 (2010) 7865–7872.
[18] L. Zhou, Z.Y. Huang, C.Z. Wang, X.X. Zhang, B.L. Xiao, Z.Y. Ma, Mech. Mater. 93 (2016) 32–42.
[19] V.C. Srivastava, V. Jindal, V. Uhlenwinkel, K. Bauckhage, Mater. Sci. Eng. A 477 (2008) 86–95.
[20] K.K. Wang, X.P. Li, Q.L. Li, G.G. Shu, G.Y. Tang, Mater. Sci. Eng. A 696 (2017) 248–256.
[21] S.D. Chen, X.H. Liu, L.Z. Liu, Trans. Nonferrous Met. Soc. China 25 (2015) 3370–3380.
[22] L. Zhou, C.Z. Wang, X.X. Zhang, B.L. Xiao, Z.Y. Ma, Acta. Metall. Sin. 51 (2015) 889–896 (in Chinese).
[23] L.Y. Qian, G. Fang, P. Zeng, L.X. Wang, Int. J. Pres. Ves. Pip. 132-133 (2015) 43–51.
[24] S. Gangolu, A.G. Rao, I. Sabirov, B.P. Kashyap, N. Prabhu, V.P. Deshmukh, Mater. Sci. Eng. A 655 (2016) 256–264.
[25] H.Z. Li, H.J. Wang, M. Zeng, X.P. Liang, H.T. Liu, Compos. Sci. Technol. 71 (2011) 925–930.
[26] C.S. Zhang, D. Jie, Y.Y. Dong, G.Q. Zhao, A.J. Gao, L.J. Wang, Int. J. Mech. Sci. 98 (2015) 195–204.
[27] Y.Z. Li, Q.Z. Wang, W.G. Wang, B.L. Xiao, Z.Y. Ma, Mater. Sci. Eng. A 620 (2015) 445–453.
[28] W.W. Peng, W.D. Zeng, Q.J. Wang, Q.Y. Zhao, H.Q. Yu, Mater. Sci. Eng. A 593 (2014) 16–23.
[29] A. Abbasi-Bani, A. Zarei-Hanzaki, M.H. Pishbin, N. Haghdadi, Mech. Mater. 71 (2014) 52–61.
[30] W.Y. Liu, H. Zhao, D. Li, Z.Q. Zhang, G.J. Huang, Q. Liu, Mater. Sci. Eng. A 596 (2014) 176–182.
[31] R. Goetz, S. Semiatin, J. Mater. Eng. Perform. 10 (2001) 710–717.
[32] G. Xiao, Q.W. Yang, L.X. Li, Trans. Nonferrous Met. Soc. China 26 (2016) 1096–1104.
[33] Y.L. Li, W.X. Wang, J. Zhou, H.S. Chen, Mater. Charact. 124 (2017) 107–116.
[34] R. Ashtiani, H.R. Parsa, M.H. Bisadi, Mater. Sci. Eng. A 545 (2012) 61–67.
[35] G.L. Ji, L. Li, F.L. Qin, L.Y. Zhu, Q. Li, J. Alloys Compd. 695 (2016) 2389–2399.